

Dynamical rearrangement of super-Earths during disk dispersal

I. Outline of the magnetospheric rebound model

Beibei Liu¹, Chris W. Ormel¹, Douglas N.C. Lin^{2,3,4,5}

¹ Anton Pannekoek Institute (API), University of Amsterdam, Science Park 904, 1090GE Amsterdam, The Netherlands

² Department of Astronomy and Astrophysics, University of California, Santa Cruz, CA 95064, USA

³ Institute for Advanced Studies, Tsinghua University, Beijing, 100086, China

⁴ Kavli Institute for Astronomy & Astrophysics, Peking University, Beijing, 100871, China

⁵ National Astronomical Observatory of China, Beijing, 100012, China

e-mail: [b.liu@uva.nl, c.w.ormel@uva.nl, lin@ucolick.org]

February 8, 2017

ABSTRACT

Context. The Kepler mission has discovered that close-in super-Earth planets are common around solar type stars. They are often seen together in multiplanetary systems, but their period ratios do not show strong pile-ups near mean motion resonances (MMRs). One scenario is that super-Earths form early, in the presence of a gas-rich disk. Such planets interact gravitationally with the disk gas, inducing their orbital migration. Disk migration theory predicts, however, that planets would end up at resonant orbits due to their differential migration speed.

Aims. Motivated by the discrepancy between observation and theory, we seek for a mechanism that moves planets out of resonances. We examine the orbital evolution of planet pairs near the magnetospheric cavity during the gas disk dispersal phase. Our study determines the conditions under which planets can escape resonances.

Methods. We extend Type I migration theory by calculating the torque a planet experiences at the interface of the empty magnetospheric cavity and the disk: the one-sided torque. We perform two-planet N-body simulations with the new Type I expressions, varying the planet masses, stellar magnetic field strengths, disk accretion rates and gas disk depletion timescales.

Results. As planets migrate outward with the expanding magnetospheric cavity, their dynamical configurations can be rearranged. Migration of planets is substantial (minor) in a massive (light) disk. When the outer planet is more massive than the inner planet, the period ratio of two planets increases through outward migration. On the other hand, when the inner planet is more massive, the final period ratio tends to remain similar to the initial one. Larger stellar magnetic field strengths result in planets stopping their migration at longer periods. We apply this model to two systems, Kepler-170 and Kepler-180. By fitting their present dynamical architectures, the disk and stellar B-field parameters at the time of disk dispersal can be retrieved.

Conclusions. We highlight *Magnetospheric rebound* as an important ingredient able to reconcile disk migration theory with observations. Even when planets are trapped into MMR during the early gas-rich stage, subsequent cavity expansion would induce substantial changes to their orbits, moving them out of resonance.

Key words. methods: numerical –planetary systems –planet–disc interactions –stars: magnetic field

1. Introduction

Together the *Kepler* and *K2* transit missions have discovered over 3 300 exoplanets and 500 multi-planet systems. These data constitute a large sample to statistically analyze the properties of exoplanets. The majority of planets discovered by Kepler are close-in super-Earths – planets with radii $R_p < 4R_\oplus$, or mass $M_p \lesssim 10M_\oplus$, and periods $P < 100$ days. Super-Earths are very common: nearly half of solar-type stars harbor a super-Earth(s) (Petigura et al. 2013). This occurrence rate appears to be independent (or at most weakly dependent) on stellar type and metallicity (Howard et al. 2012; Fressin et al. 2013; Mayor et al. 2011; Bonfils et al. 2013; Mulders et al. 2015). Several tens of super-Earths have their masses known from follow-up radial velocity or transit timing variation (Lithwick et al. 2012; Marcy et al. 2014). Combined with the radii, we are able to obtain the bulk densities. For many of them, bulk densities are too low to be consistent with a pure rocky composition: a hydrogen-helium atmosphere is required. In order to acquire such a substantial gaseous atmosphere, super-Earths are inferred to have formed in early the

gas-rich disk phase, before the depletion of the disk gas (Lopez & Fortney 2014; Rogers 2015).

Super-Earths are frequently found in multiple, compact systems with relatively low eccentricities and inclinations (Johansen et al. 2012; Fang & Margot 2012; Fabrycky et al. 2014; Shabram et al. 2016; Xie et al. 2016). Their orbits neither exhibit strong pile-ups at mean motion resonances (MMRs) nor are their period ratios uniformly distributed (see Fig. 6 of Winn & Fabrycky (2015)). In particular, the period ratio distribution shows an asymmetry around major resonances with a deficit abundance just interior to and an excess slightly exterior to the 2:1 and 3:2 MMRs. Also, a significant fraction of planets are found with period ratios much larger than 2.

Planets embedded in disks gravitationally interact and transfer angular momentum with the disk gas, resulting in their orbital migration. For low mass planets, this mechanism is known as Type I migration (Lin & Papaloizou 1979; Goldreich & Tremaine 1979; Kley & Nelson 2012; Baruteau et al. 2014). Theoretically, resonance capture is a natural outcome of planet migration (Lee & Peale 2002; Papaloizou & Szuszkiewicz 2005;

Pierens & Nelson 2008). The existence of some resonant systems, like Kepler-223 (Mills et al. 2016), proves the fidelity of disk migration theory. However, as mentioned above, statistically, the majority of super-Earths are not in MMRs. This discrepancy is a key mismatch between observation and theory.

Different scenarios have been proposed to explain the observed deviation from exact resonance. These include tidal damping of planets (Lithwick & Wu 2012; Delisle et al. 2012; Batygin & Morbidelli 2013; Lee et al. 2013; Xie 2014; Delisle et al. 2014), planet mass growth (Petrovich et al. 2013), interaction with planetesimals (Chatterjee & Ford 2015), stochastic torques in turbulent disks (Rein 2012; Batygin & Adams 2017), planet-wake interaction (Baruteau & Papaloizou 2013), and resonant overstability (Goldreich & Schlichting 2014; Delisle et al. 2015). But these models are mostly limited to small departures – at a few percent level – from resonance. Other scenarios (Ogihara & Ida 2009; Cossou et al. 2014; Ogihara et al. 2015) propose that giant impacts scatter planets away from original resonances after the dispersal of the disk gas. However, these models may not be able to explain the above asymmetry around major resonances. The onset of this orbital instability also requires a sufficient amount of embryos (typically $N \gg 2$) in a compact configuration at early stage. Nevertheless, neither of above scenarios have considered the influence of the stellar magnetic field.

T Tauri stars are magnetically active with observed field strengths of kilogauss-level at their surfaces (Johns-Krull 2007). For comparison, the *current* B-field of the Sun is only 0.3 G. The stellar magnetic field will truncate the disk at the magnetospheric cavity radius (Koenigl 1991). This radius is determined by equating the stellar magnetic torque with the viscous torque of the disk. Adopting parameters for a typical T Tauri star, the magnetospheric cavity radius is around 0.1 AU. The size of this cavity increases with time as the viscous torque diminishes during the disk dispersal. In this paper we explore how the expanding cavity affects the dynamical evolution of super-Earth planets.

We propose a new model – *magnetospheric rebound* – which considers the migration of planets near the magnetospheric cavity. Generally, during the disk dispersal, planets – trapped into MMR – can migrate outward together with the expanding magnetospheric cavity. However, when the cavity expansion rate is high or when the disk is no longer massive, the planet will be left behind. Therefore, each planet subsequently drops into the cavity at the time determined by their mass, the disk mass and the gas depletion timescale. As a consequence, planets can substantially alter their dynamical configuration with the cavity expansion during gas disk dispersal, in some cases resulting in the break-up of the MMR.

In this paper, we will test this *magnetospheric rebound* model by N-body simulations. The key parameters, apart from the planet masses, are the initial disk accretion rate, the gas disk depletion timescale, and the stellar magnetic field strength. In Sect. 2, we start by presenting the disk model and review the Type I migration torque formulas. In Sect. 3, we carry out numerical simulations and demonstrate the illustrated runs. Two observed Kepler systems are modelled in our parameter study in Sect. 4. Finally, we discuss the results and draw conclusions in Sect. 5.

2. Method

In this section, we give a description about the adopted disk model (Sect. 2.1) including the magnetospheric cavity, which truncates the disk at a radius r_c (Sect. 2.2), and provide expressions for the Type I torques that act on the planets (Sect. 2.3).

Section 2.4 outlines under which conditions the model is applicable.

2.1. Disk model

We consider a disk model with a constant aspect ratio

$$h = \frac{H}{r} = 0.025, \quad (1)$$

where H is the disk scale height and r is the disk radius. The corresponding gas disk temperature is:

$$T_g = \left(\frac{\mu h^2 G M_*}{r R_g} \right) = 150 \left(\frac{r}{1 \text{ AU}} \right)^{-1} \text{ K}, \quad (2)$$

where G is gravitational constant, R_g is gas constant, M_* is the stellar mass, and μ is the molecular weight in the protoplanetary disk. The gas surface density (Σ) is derived from the gas accretion rate \dot{M}_g by the steady-state assumption for viscous disks ($\dot{M}_g = 3\pi\Sigma\nu$). We use the Shakura & Sunyaev (1973) α prescription for viscosity, $\nu = \alpha_\nu H^2 \Omega$, where Ω is the Keplerian angular frequency. We focus on the migration of close-in super-Earths where the disk region is primarily MRI turbulent. Therefore, $\alpha_\nu = 10^{-2}$ is adopted in this paper. The gas surface density is then given by

$$\Sigma = 75 \left(\frac{\dot{M}_g}{10^{-9} M_\odot \text{ yr}^{-1}} \right) \left(\frac{\alpha_\nu}{10^{-2}} \right)^{-1} \left(\frac{r}{0.1 \text{ AU}} \right)^{-0.5} \text{ g cm}^{-2}. \quad (3)$$

Our study concerns the late phase of disk evolution when the gas disk dispersal takes place. We assume the disk gas accretion rate follows:

$$\dot{M}_g = \dot{M}_{g0} \exp[-t/\tau_d], \quad (4)$$

where τ_d is the characteristic disk depletion timescale in late stage. We note that τ_d is shorter than the typical lifetime of the disk ($\sim 2\text{-}3 \text{ Myr}$, Mamajek (2009)) by at least one order of magnitude (Williams & Cieza 2011).

2.2. Inner magnetospheric cavity

Young T Tauri stars are observed with strong magnetic fields of $\approx 0.2\text{-}6 \text{ kG}$ (Johns-Krull 2007; Yang & Johns-Krull 2011; Johns-Krull et al. 2013). The stellar magnetic field lines are strongly coupled to disk gas close to the central star. The Lorentz torque is generated by the stellar-disk magnetic interaction while the viscous torque is induced by the disk gas. The inner disk is truncated at the radius where the Lorentz torque is greater than the viscous torque (Ghosh & Lamb 1979; Koenigl 1991; Armitage 2010). The gas flow near the cavity edge is accreted onto the stellar surface along field lines, which is known as magnetospheric accretion. We assume that the gas inside the cavity ($r < r_c$) is removed very quickly, and therefore that the inner edge of the disk is sharply cut-off (see Fig. 1). The magnetic torque per unit area is $B^2 r / 2\pi$ and the viscous torque is $\dot{M}_g r^2 \Omega_K$. Assuming that the central star has a dipole magnetic field ($B(r) = B_* R_*^3 / r^3$) aligned with the stellar rotation axis, the size of this magnetospheric cavity reads (Frank et al. 1992; Armitage 2010):

$$r_c = \left(\frac{B_*^4 R_*^{12}}{4G M_* \dot{M}_g^2} \right)^{1/7}, \quad (5)$$

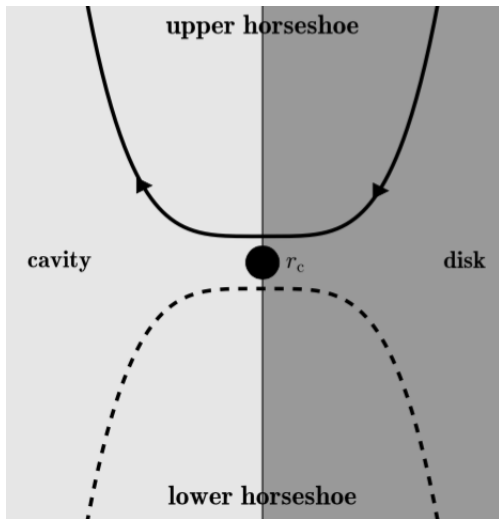


Fig. 1. Sketch of the gas motion near the cavity edge. The gas only completes the upper horseshoe U-turn before it is accreted to the central star by magneto-stellar forces, which we assume to remove the gas very quickly. There is no gas left to execute the lower horseshoe.

where G is the gravitational constant, B_* is the magnetic field strength at the stellar surface, R_* is the stellar radius and Ω_K is the angular velocity at distance r . Adopted from the fiducial value of T Tauri stars ($M_* = 1 M_\odot$, $R_* = 2 R_\odot$), Eq. (5) evaluates as

$$r_c = 0.1 \left(\frac{\dot{M}_g}{10^{-9} M_\odot \text{ yr}^{-1}} \right)^{-2/7} \left(\frac{B_*}{1 \text{ kG}} \right)^{4/7} \text{ AU.} \quad (6)$$

From Eq. (6), it is clear that the cavity expands with decreasing \dot{M}_g , a consequence of the diminishing importance of the viscous torque.

Equation (6) is based on two assumptions: (i) the stellar magnetic field is dipole; and (ii) the magnetic axis is aligned with the stellar rotation axis. In reality, the field can contain higher-order contributions, for example quadrupole term ($B_* R_*^4 / r^4$), which could dominate at stellar distances $r \sim R_*$. However, at larger distances – important for this study – the dipole contribution will take over. Also, both theoretical analyses (Lipunov & Shakura 1980; Lai et al. 2011) and MHD simulations of magnetospheric accretion (Romanova et al. 2003, 2004) indicate that when the magnetic field axis is misaligned with the rotation axis of the disk, the inner disk is likely to be warped. In that case the gas density distribution is not axisymmetric as in Eq. (3). Nonetheless, many of the features that we use in the axisymmetric case would still be present: there would still be a magnetospheric cavity, which expands during the disk dispersal, and there would still be a one-sided planet-disk interaction (as discussed in Sect. 2.3). However, to model this additional complexity is beyond the scope of this paper.

With decreasing \dot{M}_g the truncation radius (r_c) will become larger than the corotation radius r_{co} – the radius where the disk Keplerian frequency equals the spin frequency of the star. In principle, when $r_c > r_{co}$, accretion is quenched and the angular momentum is transferred from the stellar spin to the disk. However, this process also leads to a stellar spin down and the expansion of the corotation radius. Provided the disk depletion time is sufficiently long or that the spin synchronization proceeds rapidly, r_c and the corotation radius expand in tandem

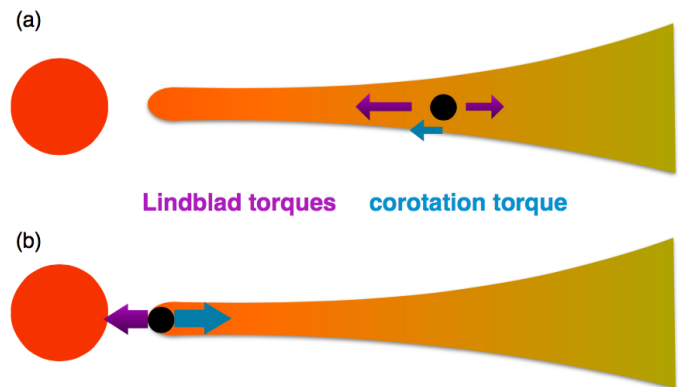


Fig. 2. Sketch illustrating the difference between two-sided and one-sided torques. (a) When the planet is far away from the disk cavity, it experiences two-sided torques. (b) When the planet is at the cavity edge, only one-sided torques operate. The purple and blue arrows denote the Lindblad and corotation torques, respectively.

and accretion onto the host star is maintained. Observationally, Kepler target stars have modest spin periods up to a few months (McQuillan et al. 2014), generally longer than the orbital periods of the inner-most super-Earths. Therefore, these systems could have experienced an expansion of the corotation radius at the time of disk dispersal. In this work we will, for simplicity, assume that the disk truncation radius is given by Equation (6) and that the disk always accretes onto the star.

2.3. Type I torques acting on the planet

Having specified a model for the gas structure, we now discuss the backreaction of the disk on the planet. The key point in our discussion is the distinction between two-sided torques and one-sided torques. A sketch illustrating the difference between one-sided and two-sided torques is given in Fig. 2. The purple and blue arrows denote the Lindblad and corotation torques, respectively. Two-sided torques apply when the planet is far from the disk cavity (Fig. 2a). In that case it experiences the inner and outer Lindblad torques from both sides. Usually, the net (differential) value is negative, causing inward migration (Ward 1997). The corotation torque is determined by the gradient of disk surface density and temperature across the horseshoe region of the planet. It is described in Sect. 2.3.1. One-sided torques are applicable when the planet is at the cavity edge (Fig. 2b). In that case it experiences a negative, one-sided Lindblad torque and a positive one-sided corotation torque. One-sided torques are generally much larger than two-sided torques, because the near-cancellation effect – a feature of the two-sided torques – is absent. The descriptions of one-sided Lindblad torque and one-sided corotation torque will be given in Sect. 2.3.2 and Sect. 2.3.3. In Sect. 2.3.4 a general Type I torque that combines these two regimes is presented.

2.3.1. Two-sided torques

When the planet is far from the disk edge and embedded in a continuous disk, the interior disk exerts a positive torque and pushes the planet outward, whereas the exterior disk pushes it inwards. To first order, these contributions cancel. The ‘standard’ two-sided Lindblad torque ($\Gamma_{L,2s}$) is therefore a differential torque with the sign being determined by the gradient of the disk

structure (Goldreich & Tremaine 1980; Tanaka et al. 2002). In addition, the planet interacts with the gas within the co-orbital horseshoe region (the two-sided corotation torque).

Considering these two torque components, we adopt the total two-sided torque from Eq. (49) of Paardekooper et al. (2010) (local isothermal approximation),

$$\begin{aligned} \frac{\Gamma_{2s}}{m_p(r_p\Omega_p)^2} &= \frac{\Gamma_{L,2s} + \Gamma_{c,2s}}{m_p(r_p\Omega_p)^2} \\ &= \left[-(2.5 + 0.5\beta + 0.1s) + 1.4\beta + 1.1\left(\frac{3}{2} + s\right) \right] q_d \frac{q_p}{h^2}, \end{aligned} \quad (7)$$

where β and s are the gradient of temperature and gas surface density, $q_d \equiv \Sigma_p r_p^2 / M_*$ and $q_p \equiv m_p / M_*$ are dimensionless measures of the local disk mass and planet mass, respectively. The notation X_p indicate quantity X evaluated at the planet location $r = r_p$. The first term on right side of Eq. (7) describes the two-sided Lindblad torque ($\Gamma_{L,2s}$) and other two terms represent the two-sided corotation torque ($\Gamma_{c,2s}$).

2.3.2. One-sided Lindblad torque

When a planet approaches the inner edge of the disk, however, the torques from the disk exterior to planet start to dominate over those from the interior disk. In the limit of a vanishing interior disk, the planet only experiences negative Lindblad torques from the exterior disk. No longer is the torque a result from a near-cancellation of two large contributions. Instead, the torque has become a first order effect. We denote this torque as $\Gamma_{L,1s}$.

The one-sided Lindblad torque can be calculated from the impulse approximation (Lin & Papaloizou 1979, 1993):

$$\Gamma_{L,1s} = -\frac{8(Gm_p)^2 r_p \Sigma_p}{9\Omega_p^2} \int_{b_{\min}}^{\infty} \frac{db}{b^4}, \quad (8)$$

where $b = r - r_p$ is the separation between each annular gas parcel and the planet and $b_{\min} = 2H/3$ is a cutoff boundary adopted for the torque density (Ward 1997; Artymowicz 1993). We then obtain for the one-sided Lindblad torque:

$$\frac{\Gamma_{L,1s}}{m_p(r_p\Omega_p)^2} = C_L q_d \frac{q_p}{h^3}, \quad (9)$$

where the prefactor $C_L = -0.65$.

2.3.3. One-sided corotation torque

We next calculate the corotation torque when the planet is at the cavity edge. In the context of a co-rotation torque with one-sided, it means that only the upper horseshoe is present (where material is transported from orbits exterior to the planet to orbits interior to the planet; see Fig. 1). The lower horseshoe motion is absent by virtue of the assumption that any gas interior to the planet is quickly removed along magnetic field lines and accreted to the central star. Therefore, the planet exchanges angular momentum only through the upper horseshoe, which provides a strong positive corotation torque. We denote this torque the one-sided corotation torque $\Gamma_{c,1s}$. It can be calculated from angular momentum conservation principles, i.e., the angular momentum lost due to material being pushed to a lower Keplerian orbit is gained by the planet. Following Paardekooper & Papaloizou (2009a):

$$\Gamma_{c,1s} = \int_0^{x_{\text{hs}}} \Sigma(j - j_p)(\Omega - \Omega_p)r \, dr = \frac{1}{2}(\Omega_p r_p)^2 \Sigma r_p^2 x_{\text{hs}}^3, \quad (10)$$

where $j = \Omega_K(r)r^2$ is the specific angular momentum corresponding to r . We adopt $x_{\text{hs}} = 1.7(q_p/h)^{0.5}r_p$ (Paardekooper & Papaloizou 2009b; Ormel 2013) for the half-width of the horseshoe region and obtain

$$\frac{\Gamma_{c,1s}}{m_p(r_p\Omega_p)^2} = C_{\text{hs}} q_d \left(\frac{q_p}{h^3}\right)^{1/2}, \quad (11)$$

where $C_{\text{hs}} = 2.46$.

Based on the assumption that gas is removed quickly at the edge of the disk, the surface density has a infinite sharp transition at r_c . Under this assumption, the planet obtains its maximum positive one-sided corotation torque and it maximizes the rebound (outward migration). For simplicity, we only consider this situation. Instead, if gas removal is not an efficient process, there could be a more gradual transition, with Σ being (locally) a power-law. In that case, the Lindblad and corotation torques at r_c are determined by the two-sided torques expression, which reduces (but does not diminish) the rebound. Three-dimensional MHD simulations of magnetospheric accretion (Romanova et al. 2002) nevertheless reveal a strong cut-off of the gas density near the disk edge, supporting our approximation.

The migration rate corresponding to a torque (Γ) is

$$\frac{\dot{a}}{a} = \frac{2\Gamma}{m_p r_p^2 \Omega_p}. \quad (12)$$

In Fig. 3, the migration rate (\dot{a}/a) is plotted for the two-sided torque Γ_{2s} , the one-sided corotation torque $\Gamma_{c,1s}$, the one-sided Lindblad torque $\Gamma_{L,1s}$ as function of q_p at $r = 0.1$ AU. The dark grey zone refers to the non-linear regime and the light grey zone indicates the gap opening regime (see the discussion in Sect. 2.4). Two-sided torques are second order torques, which sign depends on the gradient of the disk profile in the vicinity of the planet (Eq. (7)). But one-sided torques are independent of s and β (Eq. (11) and Eq. (9)). Indeed, one-sided torques are larger than two-sided torques (approximately by a factor h^{-1}). Between the one-sided torques, the positive corotation torque is larger than the negative Lindblad torque when q_p is small. Recall that the one-sided torques operate for the disk region near the cavity whereas the two-sided torques operate for the disk region away from the cavity. Therefore, small planets are able to migrate outward from the disk edge until the point where the two-sided torques dominate. This also means that small planets would migrate outward when the cavity gradually expands.

However, when the planet is large enough to enter the gap-opening regime, the corotation torque diminishes due to the depletion of gas in the horseshoe region. Then, the (negative) one-sided Lindblad torque would be in magnitude larger than the (positive) one-sided corotation torque. In that case, the planet directly migrates into the cavity and is left behind as the disk cavity (r_c) expands.

Since the eccentricities of planets could be excited by planet-planet interaction, we also consider the saturation of the corotation torque (both one-sided and two-sided) (Bitsch & Kley 2010):

$$\Gamma_c(e) = \Gamma_c(0) \exp[-e/e_f], \quad (13)$$

where e is the eccentricity of the planet, $\Gamma_c(0)$ is the corotation torque for zero eccentricity, and $e_f = h/2 + 0.01$ (Fendyke & Nelson 2014).

2.3.4. Combined Type I torque

A more general case applies when a planet approaches the disk edge, which falls in between the one-sided and embedded (two-

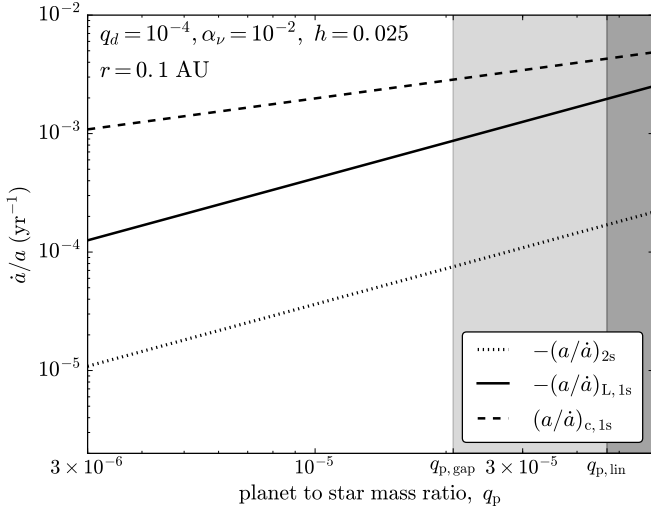


Fig. 3. Planet migration rate (\dot{a}/a) for different torques as a function of dimensionless planet mass $q_p = M_p/M_*$ at $r = 0.1$ AU. The dotted, solid and dashed lines correspond to the migration rate estimated from Eq. (12) when $\Gamma = \Gamma_{2s}$ (two-sided torque), $\Gamma_{L,1s}$ (one-sided Lindblad torque) and $\Gamma_{c,1s}$ (one-sided corotation torque), respectively. The dark grey zone refers to the non-linear regime, and the light grey zone indicates the gap opening regime. $q_{p,\text{gap}}$ and $q_{p,\text{lin}}$ are the critical masses for these two regimes (see Sect. 2.4). The adopted disk parameters are $q_d = 10^{-4}$, $\alpha_\nu = 10^{-2}$ and $h = 0.025$.

sided) regimes discussed above. In that case, the torque expression is approximated by interpolating the one-sided and two-sided torques:

$$\Gamma = \begin{cases} f\Gamma_{1s} + (1-f)\Gamma_{2s} & \text{when } r \geq r_c \\ 0 & \text{when } r < r_c \end{cases} \quad (14)$$

where the coefficient $f = \exp[-(r - r_c)/x_{\text{hs}}]$ is a measure for the proximity of a planet to the disk edge ($f = 1$: at the edge; $f = 0$: far away from the edge). The form of the expression ensures that the total torque is dominated by the one-sided torque when the planet is located within a half-horseshoe width from the disk edge ($r_p \leq r_c + x_{\text{hs}}$).

2.4. Model applicability

Our expressions for the Type-I torques are valid in the linear regime where the planet's perturbation is small. This requires the planet Hill radius to be smaller than the disk scale height ($R_H \equiv (m_p/3M_*)^{1/3} < H$, Lin & Papaloizou (1993)). This condition can be expressed as

$$q_p \lesssim 3h^3 = 4.7 \times 10^{-5} \left(\frac{h}{0.025} \right)^3 \quad (15)$$

The no-gap opening criterion also requires that the planet torque (Γ_p) is smaller than the viscous torque ($\Gamma_\nu = 3\pi\Sigma\nu r^2\Omega$). Otherwise the disk does not supply enough material (angular momentum) to fuel the planet. This condition is especially relevant to planets at the disk edge r_c where the planet torque is dominated by the 1-sided corotation torque, $\Gamma_p = \Gamma_{c,1s}$ (Eq. (11)). The no-gap opening condition reads

$$\left(\frac{q_p}{h^3} \right)^{3/2} \lesssim \frac{3\pi\alpha_\nu}{C_{\text{hs}}h}, \quad (16)$$

or

$$q_p \lesssim 2.1 \times 10^{-5} \left(\frac{h}{0.025} \right)^{7/3} \left(\frac{\alpha_\nu}{10^{-2}} \right)^{2/3}. \quad (17)$$

For typical super-Earth planets ($M_p \lesssim 10 M_\oplus$) around solar type stars, the above two conditions require $h \gtrsim 0.025$ near the edge of the disk. In addition, the no-gap opening condition requires a large α_ν parameter. This explains our default values for h and α_ν . The $\Gamma_{c,1s}$ is the torque that provides planet outward migration nearly the cavity edge. For very low h and α_ν disks, gaps can be opened by super-Earth planets. Γ_c is reduced since the gas is severely depleted in their horseshoe regions. As a consequence, we do not expect the magnetospheric rebound mechanism to operate in systems with low h and α_ν .

But how realistic are our adopted values of h and α_ν ? Typically, MHD simulations modelling the MRI (Balbus & Hawley 1998) indicate $\alpha \simeq 10^{-2}$ (Davis et al. 2010; Suzuki et al. 2010), provided the disk is sufficiently ionized. Generally, this holds true for the very inner disk ($\gtrsim 10^3$ K) where thermal ionization of alkali elements produce the required amount of electrons (Armitage 2011). As the cavity radius (r_c) expands, however, the temperature drops and ionization becomes dependent on non-thermal processes (e.g., stellar X-ray irradiation). Although initially the high densities should prevent X-rays from penetrating the disk midplane, the expansion of the cavity radius also quickly decreases Σ since $\Sigma(r_c) \propto r_c^{-4}$ (see Eqs. (3) and (5)). In addition, we note that because we study the inner disk ($a \lesssim 0.3$ AU) at late times, small dust grains have coagulated into large bodies. In such a dust-free medium the liberated electrons always end up in the gas, increasing the electron fraction and promoting the MRI.

The disk's aspect ratio is determined by a thermal balance: an increased midplane temperature increases h (Eq. (2)). A high midplane temperature can result from viscous dissipation (a high \dot{M}) in combination with a large vertical optical depth. But as the disk evolves at late stage, a higher T can also arise when the (visible) optical depth is low and stellar photons penetrate the disk deeper. For example, in the optically thin limit, the equilibrium temperature at 0.1 AU for a solar mass star would be 1200 K, corresponding to a scale height of 0.022. In addition, magnetic accretion generates additional heat near the cavity edge (Hartmann et al. 1998), further increasing the aspect ratio h .

Based on these considerations, we believe that the adopted values of $h = 0.025$ and $\alpha = 10^{-2}$ are reasonable. Note that we assume a constant aspect ratio in this paper, which is independent of r . Another aspect ratio profile, $h = 0.05r^{1/5}$, has also been investigated and we find that the results presented in the following sections are only weakly affected. Overall, our results should be applicable to super-Earth planets as long as the inner disk is indeed hot enough.

In addition, the magnetospheric accretion process requires efficient coupling between the field lines and the disk gas. This condition implies that the magnetic diffusivity η is sufficiently small, $\eta \lesssim Hc_s$ (Wardle 2007). The criterion for the onset of MRI is that the magnetic Reynolds number is larger than 1, $Re_M = v_A H / \eta = \alpha_\nu^{1/2} H c_s / \eta \gtrsim 1$ (Armitage 2010), where c_s and v_A are the sound speed and Alfvén speed. This suggests $\eta \lesssim \alpha_\nu^{1/2} H c_s$. Therefore, the disk always satisfies the coupling condition once the MRI is operational. The model is applicable since we study super Earth systems with typical orbital periods of a few weeks around their host stars.

Ogihara et al. (2010) also calculate a torque near the disk edge, which they term the ‘edge torque’. This torque operates

for eccentric planets at the disk edge, which experience asymmetric eccentricity damping from the disk gas. The magnitude of the edge torque increases with the eccentricity of the planet. However, when calculating the total torque in their Eq. (17), they still use the two-sided Type I torque expression. As we demonstrate in this paper, when the planet is near the disk edge, one-sided torques will dominate over two-sided torques. Also, we find that the eccentricities of the planets are modest (a few times 10^{-2}) in our simulations. For these low eccentricities, the one-sided torque (Eq. (11)) is much larger than the edge torque (Eq. (15) of Ogihara et al. (2010)). We therefore neglect the edge torque in this paper.

3. Results

We carry out numerical experiments on Hermite N-body code (Aarseth 2003). In this code, the planet-planet interaction is calculated with Hermite scheme, and the planet-disk interaction is included by adding additional torque recipes (See details in Liu et al. (2015)). However, Liu et al. (2015) only consider the two-sided torques (Paardekooper et al. 2011). In this work, we add the new torque formulas demonstrated in above section, which is a combination of both one-sided and two-sided torques. A further difference is that this work considers in the locally isothermal limit, which is applicable to the late disk dispersal phase when the disk opacity is substantially reduced.

The goal of our simulations is to investigate the evolution of the period ratio of the planet pair during the dispersal of the gas disk. In this paper, only two-planet systems are considered. The simulations are performed until the disk gas is entirely depleted. Because the long-term secular evolution of a two-planet system would not change their orbits once the planets are in the Hill stable regime, we can consider the orbits of planets at the end of simulations as their present-day orbits. A set of simulations (referred to as run 1–4) with different planet masses (M_{in} and M_{out}), disk properties (\dot{M} , τ_d), and stellar magnetic field strength (B_*) are performed. We set $M_* = 1 M_\odot$ throughout this section. The adopted parameters are given in Table 1 and the results are illustrated in Fig. 4.

3.1. Planet pair with massive outer one

The result from the default run is presented in Fig. 4a. The parameters are set as $\dot{M}_{g0} = 10^{-8} M_\odot \text{ yr}^{-1}$, $\tau_d = 10^5 \text{ yr}$ and $B_* = 1 \text{ kG}$. The black solid lines show the time evolution of embryos' semimajor axes and the blue dashed line represents the expansion of r_c . Initially, the magnetospheric cavity radius (r_c) is at 0.052 AU and two embryos are located at 0.052 AU and 0.076 AU. Their orbits are hence initialized between the 3:2 and 2:1 MMR. The inner and outer planet masses are $3 M_\oplus$ and $6 M_\oplus$.

Because of convergent migration, the planets soon get trapped into the 3:2 MMR and migrate inward to the magnetospheric cavity within a few thousand years. When the inner planet gets close to the cavity edge ($r_{\text{in}} \simeq r_c$), one-sided torques become dominant. For this combination of disk and planet parameters, the outward (positive) one-sided horseshoe torque is larger in magnitude than the inward (negative) one-sided Lindblad torque ($\Gamma_{1s,hs} + \Gamma_{1s,L} > 0$). Since the outer planet is far away from the disk edge in terms of horseshoe units, $(r_{\text{out}} - r_c)/x_{hs} \gg 1$, its torque is still in the 2-sided regime and negative. However, the sum of the torques on both planets

is dominated by the one-sided torque from the inner planet and evaluates to a net positive value.

Whether or not the planet pair migrates outward is determined by two timescales: the planet migration timescale τ_m ($= (\dot{a}/a)^{-1}$, see Eq. (12)) and the cavity expansion timescale τ_c (which approximately equals $3.5\tau_d$, see Eq. (6)). If the cavity expands at a speed much larger than the migration of the planet, it overtakes the planet. The planet would then fall into the cavity and cease migrating. Otherwise, when $\tau_m < \tau_c$, it keeps migrating with the expansion of the cavity. Because $\tau_m < \tau_c$ initially, the total disk torques drive the outward migration of both planets. However, as $\dot{M}_g(t)$ decreases with time, the disk gas mass diminishes, which increases the migration time τ_m . Therefore, at some point $\tau_m(t)$ becomes longer than τ_c , which indicates that the disk can no longer accommodate the migration of both planets. The inner planet therefore drops into the inner cavity radius r_c (blue dashed line in Fig. 4). We find that this occurs at $t_1 = 3.0 \times 10^5 \text{ yr}$.

After $t = t_1$ the planet pair initially moves inward, because the net torque is now due to the outer planet and the planets are still in resonance. However, the planet pair decouples from MMR when the expanding cavity approaches the outer planet ($r_{\text{out}} \simeq r_c$). After that, only the outer planet is able to migrate outward with the cavity expansion. This is because divergent migration leads to resonance crossing rather than resonance trapping (Henrard & Lemaître 1983; Murray & Dermott 1999). Eventually, it ceases migrating at around $5.6 \times 10^5 \text{ yr}$ when the migration timescale of the outer planet becomes longer than the cavity expansion timescale. We denote this time t_2 . After $t = t_2$ both planets are within the magnetospheric cavity.

After the gas is entirely depleted, the planets end up at 0.116 AU and 0.254 AU. Their final outer-to-inner period ratio ($P_{\text{out}}/P_{\text{in}}$) is 3.24, much larger than the original 3:2 resonance.

3.2. System with more massive inner planet

We show the result of run 2 in Fig. 4b. It has identical model parameters as the default run, but the mass order of the planets is changed: $M_{\text{in}} = 6M_\oplus$ and $M_{\text{out}} = 3M_\oplus$.

Similar to run 1 initially both planets migrate to the cavity edge in the 3:2 MMR. Also, the migration timescale for the pair (τ_m) is likewise shorter than τ_c , so both planets migrate outward with the expansion of the cavity. After a while, the inner planet ceases migrating when the expansion rate of the cavity starts to exceed the migration rate of the two resonant planets. This occurs at $t_1 = 4.6 \times 10^5 \text{ yr}$. It is later than the time in run 1 ($3.0 \times 10^5 \text{ yrs}$). When the cavity radius r_c approaches the outer planet at $t_2 = 5.7 \times 10^5 \text{ yr}$, it directly falls in, without substantial outward migration as run 1. Consequently, their final period ratio $P_{\text{out}}/P_{\text{in}} = 1.57$, is still close to the 3:2 MMR.

Why are the final period ratios between run 1 and run 2 so different when only their mass ratio has changed? The small outer-to-inner mass ratio in run 2 has two significant effects. First, the torques' contribution from the inner massive planet becomes even more dominant. It means that the inner planet falls into the cavity at a later time (t_1 in run 2 is larger). Therefore, both planets migrate further out when the inner planet is more massive. A second consequence is that r_c only approaches the outer planet at a late time when the disk mass is relatively low. A low disk mass and a less massive outer planet leads to subsequent slow outward migration. As a consequence, in run 2, the migration timescale of the outer planet is longer than the cavity expansion timescale when the cavity approaches it. Hence, the

Table 1. Adopted parameters

Run	Name	M_{in} (M_{\oplus})	M_{out} (M_{\oplus})	\dot{M}_{g0} ($M_{\odot}\text{yr}^{-1}$)	τ_d (yr)	B_* (kG)	Period ratios	
							Initial	Final
#1	Default	3	6	10^{-8}	10^5	1	1.75	3.24
#2	Massive inner	6	3	10^{-8}	10^5	1	1.75	1.57
#3	Strong B_*	3	6	10^{-8}	10^5	5	1.75	3.23
#4	Light disk	3	6	5×10^{-10}	10^4	1	1.75	1.72

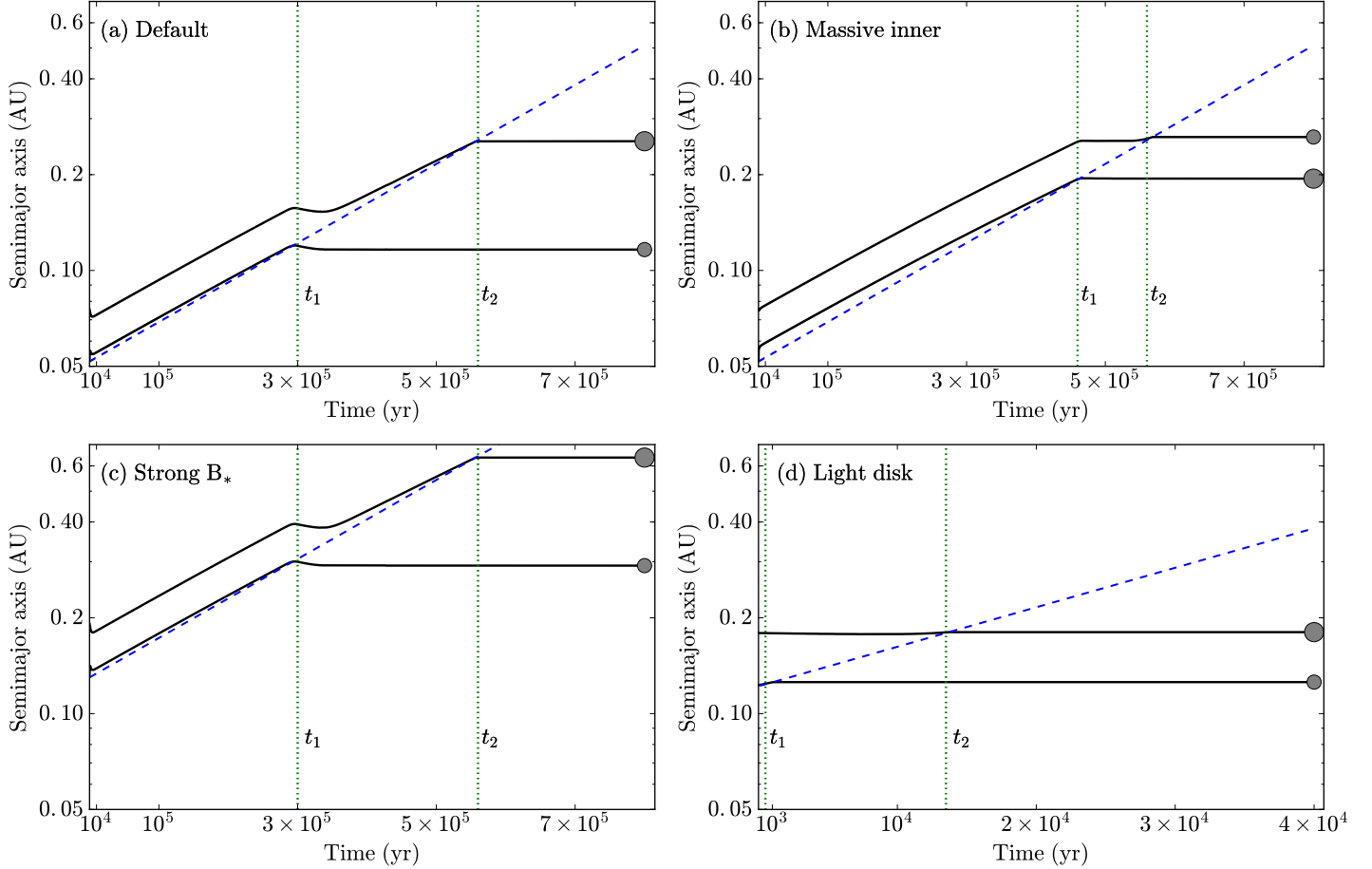


Fig. 4. Migration of a planet pair in the gaseous disk. Black lines trace the time evolution of the semi-major axes of the planets and the blue dashed line represents the inner magnetospheric radius r_c . The four panels show simulations with (a) default parameters, (b) massive inner planet, (c) strong stellar magnetic field and (d) a light disk. Parameters are listed in Table 1. The vertical lines represent the time when the inner (t_1) and the outer planet (t_2) enter the cavity. Note that the the scale of the x-axis of panel (d) is different from the others.

outer planet drops into the cavity, and their orbits still remain close to the 3:2 MMR.

3.3. Strong stellar magnetic field

We perform run 3 with the same planet masses and disk parameters as the default run, but a stronger stellar magnetic field of $B_* = 5$ kG. The result is presented in Fig. 4c. For this strong B-field, $r_c = 0.13$ AU at the beginning. This is because the magnetospheric cavity is determined by the dominated stellar magnetic torque. As shown in Eq. (6), larger B_* results in a stronger magnetic torque that truncates the inner disk further out. The embryos' migration behaviours are similar to the default run. They enter into the cavity at the same time (t_1 and t_2) and stop at the same period ratio as run 1. The reason is that the time when

the planets enter the cavity depends on the comparison between planet migration timescale and the cavity expansion timescale – both of which are independent of the B_* . However, the stronger B-field carries the planets further away, with the final orbits of the two planets ending up at 0.292 AU and 0.637 AU.

3.4. Light disk

Finally, we perform a run with same planet masses as run 1 ($M_{\text{in}} = 3 M_{\oplus}$, $M_{\text{out}} = 6 M_{\oplus}$) but different disk parameters ($\dot{M}_{g0} = 5 \times 10^{-10} M_{\odot}\text{yr}^{-1}$, $\tau_d = 10^4$ yr). Here the initial disk accretion rate (\dot{M}_{g0}) decreases by a factor of 20 and the disk depletion time (τ_d) reduces by a factor of 10. Low \dot{M}_{g0} indicates that the initial disk mass is low and short τ_d means that the gas is depleted rapidly. The combination of these two parameters im-

plies a light disk (small Σ or q_d) during the evolution timespan simulated here. In contrast to the massive disk in the default run, the light disk can not provide sufficient angular momentum exchange to the planets. Therefore, the planet migration timescale τ_m is always longer than the cavity expansion timescale τ_c in this case. Both planets result in only minimal change of their orbits. The final period ratio of the planet pair is 1.72, very close to its initial value (see Fig. 4d).

4. Modelling Kepler Systems

The goal of this section is to compare the observed super-Earth systems with our proposed *magnetospheric rebound* model. In order to investigate under which conditions these systems preferentially form, we conduct a parameter study, varying \dot{M}_g , τ_d and B_* .

4.1. Set-up for the parameters survey

For our pilot study, we consider two super-Earths systems: Kepler 170 and Kepler 180. Kepler 170 contains two super-Earth planets near the 2:1 MMR, whereas the period ratio of the planets in Kepler 180 is 3.03. Theoretically, planet migration theory dictates that planets – when formed in gas-rich disks – are likely to end up in MMR. However, the Kepler mission has shown that many super-Earths are at period ratios near but not exactly at MMR (e.g., 2.2:1; Steffen & Hwang 2015), or that their period ratios are far from any MMR. Motivated by the representative period ratios of these two systems, we select them as typical cases and explore why the planets end up so differently.

The planet masses and their periods, the stellar masses are listed in Table 2. The observed systems are selected from the NASA Exoplanet Archive (<http://exoplanetarchive.ipac.caltech.edu/>), their planet masses are obtained from Wolfgang et al. (2016)'s mass-radius relationship (their Eq (1)):

$$M_p/M_\oplus = 2.1(R_p/R_\oplus)^{1.5} \quad (18)$$

All planets are initialized in coplanar and circular orbits. The inner planet is located at the edge of the inner cavity, and the outer planet starts beyond their 2:1 MMR.

The initial gas accretion (\dot{M}_g) rate is sampled by 5 values in the range of 10^{-9} to $10^{-7} M_\odot \text{yr}^{-1}$, the disk dispersal time (τ_d) is given by 3 values, 10^3 , 10^4 , 10^5 yr, and the magnetic field strength (B_*) is selected from 3 values, 0.3, 1, 3 kG. We run 45 simulations for each system with each simulation referring to one specific combination values of \dot{M}_{g0} , τ_d and B_* . Their outcomes ($P_{\text{out}}/P_{\text{inn}}$ and P_{inn}) are given in Fig. 5. The left and right panel show the results of Kepler 170 Kepler 180, respectively. The color, size and shape of the data points refer to τ_d , B_* and \dot{M}_{g0} , respectively. The red star marks the location of the observed systems in this $P_{\text{out}}/P_{\text{inn}} - P_{\text{inn}}$ diagram.

4.2. Kepler 170

Kepler 170 is a $0.97 M_\odot$ star, containing two super-Earth planets, Kepler 170b and Kepler 170c. Based on the radius from the transit and mass-radius relation from Eq. (18), the masses of the planets are $10.59 M_\oplus$ and $9.42 M_\oplus$, respectively. Their periods are 7.93 and 16.67 days, with a period ratio of 2.10.

For this system the simulated data results in a large spread in the period of the inner planet (x-axis of Fig. 5a): P_{inn} ranges

from 1.2 to 68 days. With tuning of the parameters, we can easily obtain a perfect match to the inner planet period. Although the simulated period ratios all lie below the observed value, five of them showing only minor deviation ($\approx 1.3\%$). Note that all five yellow triangles with different size are stacked at the same period ratio close to 2.07. One may wonder that the simulations cannot reproduce period ratios larger than the observed one. The reason is the empirical mass-radius relationship used here (Eq. (18)). Because of the uncertainty in $M(R)$, the true mass likely deviates from the estimated value. However, a slightly higher outer-to-inner mass ratio – still consistent with the observational constraints – will result in a period ratio that matches the observed value.

In Fig. 5a, we see that for the same initial disk accretion rate and gas depletion timescale (the same size and color), the inner planet period is longer when the stellar B-field is stronger (triangles lie left of circles). This can be understood from our previous discussion related to Fig. 4a and c: larger stellar magnetic field strength results in planets stopping their migration at longer periods, because the disk cavity radius r_c is further out.

We also see that for the same gas depletion timescale and stellar B-field but for increasing \dot{M}_{g0} (same symbols from small to large along the lines) the period ratio increases from 2 to ≈ 2.07 . Because planets get trapped into the 2:1 MMR first, they migrate outward and leave resonance through the cavity expansion. A high \dot{M}_{g0} results in substantial outward migration and hence increases their period ratio. An exception are the runs with the strongest stellar B-field (circles). Their final period ratios decrease from 2 to ≈ 1.8 with increasing \dot{M}_{g0} (large circles in lower right corner of Fig. 5a). The reason is that these planets, *before* the magnetospheric rebound, got trapped in 3:2, instead of 2:1. Because resonance trapping is related to the migration rate, only planets with fast migration rates (meaning: large local disk mass $\Sigma_p r_p^2$, Eq. (12)) are able to bypass the resonance barrier (Ogihara & Kobayashi 2013; Liu et al. 2015, 2016). Both a higher disk accretion rate (larger Σ_0) and a larger stellar B-field (larger r_p) contribute towards increasing the local disk mass. Therefore, only systems with \dot{M}_{g0} and large B_* are able to bypass the 2:1 MMR and be trapped into the 3:2 MMR. Finally, *magnetospheric rebound* pushes the resonant planets outward and increase the period ratio from the 3:2 MMR to a value between 1.5 to 2 during the disk dispersion phase.

The interpretation of this particular system is applicable to systems that contain nearly equal-mass super-Earths, close to 10 days inner planet period, and period ratio slightly in excess of 2. These systems follow a similar formation history, and their B_* , τ_d and \dot{M}_{g0} can be modelled with the same approach shown here.

4.3. Kepler 180

Kepler 180 is a $1.05 M_\odot$ star and harbors two super-Earths: Kepler 180b and Kepler 180c. The masses of the planets are $3.90 M_\oplus$ and $9.27 M_\oplus$, and their periods are 13.82 and 41.89 days, respectively. Their outer-to-inner mass ratio is 2.38 and their period ratio is 3.03. Its result is presented in Fig. 5b.

One obvious difference between Fig. 5a and b is that the period ratios of simulated planets in Fig. 5b ($\gtrsim 2$) can be much larger than those of Fig. 5a (~ 1.7 -2.1). Although the planets get quickly trapped into MMR, they move away from resonance during the magnetospheric cavity expansion. We can understand this behavior from the simulations conducted in Fig. 4a and Fig. 4b (Run #1,2). There, the only difference is the mass or-

Table 2. Properties of observed super-Earth system

Name	Stellar mass (M_\odot)	$R_{\text{inn}}, R_{\text{out}}$ (R_\oplus)	$M_{\text{inn}}, M_{\text{out}}$ (M_\oplus)	$P_{\text{inn}}, P_{\text{out}}$ (day)	$P_{\text{out}}/P_{\text{inn}}$
Kepler 170	0.97	2.94, 2.72	10.59, 9.42	7.93, 16.67	2.10
Kepler 180	1.05	1.51, 2.69	3.90, 9.27	13.82, 41.89	3.03

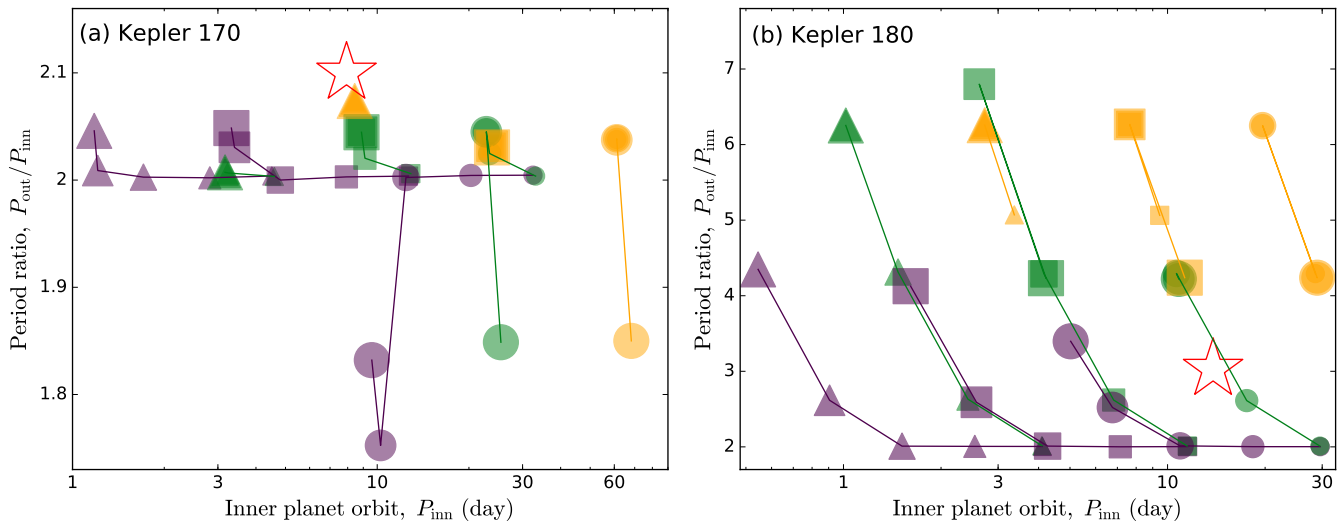


Fig. 5. Scatter plot of the inner period of the planet and the period ratio of the outer-to-inner planet. The left and right panel present the results of Kepler 170 and Kepler 180. The red star represents the observed data and other symbols give the results of numerical simulations. Symbols correspond to stellar magnetic field strengths B_* where B_* equals 0.3 kG (triangle), 1 kG (square) and 3 kG (circle). Color corresponds to the disk dispersal timescale (τ_d) where purple, green, orange mean 10^3 , 10^4 and 10^5 yr. The size of the symbols represent the disk accretion rate at the onset of disk dispersal (\dot{M}_{g0}), ranging from 10^{-9} (small), 3×10^{-9} , 10^{-8} , 3×10^{-8} to $10^{-7} M_\odot \text{yr}^{-1}$ (large).

der of the planets. When the outer-to-inner planet mass ratio is large, the outer planet can continue to migrate extensively after leaving resonance, resulting in a large period ratio. In Kepler 180 the outer planet is more massive than the inner one, whereas in Kepler 170 the planets are of nearly equal-mass. Consequently, the period ratios in Fig. 5b are larger than those in Fig. 5a.

From Fig. 5b we see that the observed planet periods and their ratio (red star) lie inside the range spanned up by the simulations. Therefore, this system is well-fitted by the *magnetospheric rebound* mechanism and we are able to constrain key disk and stellar magnetic parameters. Kepler 180 represents the systems that have a massive outer planet ($M_{\text{out}}/M_{\text{inn}} \gtrsim 2$) and typical period ratio larger than ~ 2.5 . These super-Earths are far from first order resonance – a feature that cannot be explained by convergent migration alone. The *magnetospheric rebound* mechanism that we propose, however, is able to explain the formation of these type of systems.

5. Discussion and Conclusion

In this paper, the *magnetospheric rebound* mechanism has been developed to explain the departure of close-in super-Earths from resonance. *Magnetospheric rebound* relies on the outward migration of planets that end up near the magnetospheric cavity radius. At this radius (the disk edge) the Type I torque becomes one-sided. We have derived the expression for the one-sided corotation torque (Eq. (11)) for the first time. We have performed N-body simulations of the dynamical evolution of two-planet systems during the gas disk dispersal phase, varying the planet masses (M_p), the disk accretion rate (\dot{M}_{g0}), the disk depletion timescale (τ_d) and the stellar magnetic field strength (B_*). We

find that the final orbits of the planets can be substantially rearranged by the magnetospheric cavity expansion. Three major features of our study are:

1. The disk significantly affects the migration behavior and, consequently, the final period ratio of the planets. The outward migration of the planet with the expanding cavity is substantial in a massive disk (high \dot{M}_g , long τ_d). On the other hand, light disks cannot transfer sufficient angular momentum to the planets (low \dot{M}_g , short τ_d). Planets in light disks therefore tend to remain at the orbits they had before the onset of the disk dispersal.
2. When the outer planet is more massive than the inner one ($M_{\text{out}} > M_{\text{in}}$), the planets tend to move away from their original resonance state. In contrast, when the inner planet is more massive ($M_{\text{out}} < M_{\text{in}}$), their final period ratio remains similar to the initial one the planets had at the onset of the disk dispersal.
3. The strength of the stellar magnetic field (B_*) determines the size of the cavity and consequently affects the planets' final locations. The planets end up at a longer period when the B-field of the central star is stronger.

As described in Sect. 2.4, our model is limited to the linear approximation of super-Earths (Eq. (15)) and the non-gap opening criterion (Eq. (16)). These conditions restrict our model to low-mass planets ($M_p \lesssim 10M_\oplus$ for solar-type stars), hot and turbulent inner disks ($h \gtrsim 0.025$ and $\alpha_\nu \gtrsim 10^{-2}$). Therefore, magnetospheric rebound is inapplicable to massive giant planets around solar-type stars, and super-Earths around very low mass stars.

Although only two-planet systems are considered in this paper, it is straightforward to extend our model to systems with more than two planets. The timescales analysis (migration timescale of planets vs. cavity expansion timescale) given in Sect. 3 is still applicable to those systems. However, for >2 planets dynamical instability may be triggered after the disk is entirely dispersed. Therefore, for >2 planet systems the long-term ($\sim G_{\text{yr}}$) secular evolution must be considered. In this paper where we consider only two-planet systems, the problem of post-disk dynamical instability does not arise, because our two-planet systems are Hill stable. Specifically, Hill stability is assured when the planets' mutual separation is larger than $2\sqrt{3}R_{\text{H}}$ ($P_{\text{out}}/P_{\text{inn}} \gtrsim 1.06$ for typical super-Earth) (Gladman 1993). This condition is always satisfied for the planets at the end of our simulations.

Overall, our model provides a new direction for studying the dynamics of the super-Earths. For the first time, we have included the effects of the stellar magnetic field, the dispersal of the gas disk and planet migration into one unified model. Even when planets trap into MMRs due to disk migration in the early gas-rich phase, subsequent disk dispersal will induce diversity in their orbital configurations. Therefore, super-Earths can form early and yet escape resonance – a scenario consistent with both migration theory as well as the Kepler census.

Applying the *magnetospheric rebound* model to Kepler 170 and Kepler 180, we were able to constrain the formation conditions (e.g., $\dot{M}_{\text{g}0}$, τ_{d} and B_*) that result in an architecture consistent with the observations (Section 4). In addition, our results hint that a two-planet system will end up with a period ratio that depends on the mass order of the planets (Section 3). However, to ultimately verify the *magnetospheric rebound* model, a statistical analysis is needed. Specifically, the Kepler mission has vastly increased the number of multi-planetary systems. Therefore, a large sample is available to statistically analyze the orbital properties of the super-Earth population. In a follow-up paper, we will conduct a full exploration of this mass ratio-period ratio correlation in the light of two formation scenarios of super-Earths (Morbidelli & Raymond 2016): *in-situ* growth (Hansen & Murray 2012; Chiang & Laughlin 2013) and migration (Terquem & Papaloizou 2007; McNeil & Nelson 2010). Comparison between the predictions of the magnetospheric rebound model and the Kepler observations enable us to distinguish between these formation scenarios, and to gain a better understanding of the origin of super-Earths.

Acknowledgements. We thank Shigeru Ida, Carsten Dominik, Gijs Mulders, Bin Dai and Zhuoxiao Wang for useful discussions. We also thank the anonymous referee for their helpful suggestions and comments. B.L. and C.W.O are supported by the Netherlands Organization for Scientific Research (NWO; VIDI project 639.042.422).

References

Aarseth, S. J. 2003, *Gravitational N-Body Simulations*, 430
 Armitage, P. J. 2010, *Astrophysics of Planet Formation*, 294
 Armitage, P. J. 2011, *ARA&A*, 49, 195
 Artymowicz, P. 1993, *ApJ*, 419, 155
 Balbus, S. A. & Hawley, J. F. 1998, *Reviews of Modern Physics*, 70, 1
 Baruteau, C., Crida, A., Paardekooper, S.-J., et al. 2014, *Protostars and Planets VI*, 667
 Baruteau, C. & Papaloizou, J. C. B. 2013, *ApJ*, 778, 7
 Batygin, K. & Adams, F. C. 2017, *ArXiv e-prints*
 Batygin, K. & Morbidelli, A. 2013, *AJ*, 145, 1
 Bitsch, B. & Kley, W. 2010, *A&A*, 523, A30
 Bonfils, X., Delfosse, X., Udry, S., et al. 2013, *A&A*, 549, A109
 Chatterjee, S. & Ford, E. B. 2015, *ApJ*, 803, 33
 Chiang, E. & Laughlin, G. 2013, *MNRAS*, 431, 3444

Cossou, C., Raymond, S. N., Hersant, F., & Pierens, A. 2014, *A&A*, 569, A56
 Davis, S. W., Stone, J. M., & Pessah, M. E. 2010, *ApJ*, 713, 52
 Delisle, J.-B., Correia, A. C. M., & Laskar, J. 2015, *A&A*, 579, A128
 Delisle, J.-B., Laskar, J., & Correia, A. C. M. 2014, *A&A*, 566, A137
 Delisle, J.-B., Laskar, J., Correia, A. C. M., & Boué, G. 2012, *A&A*, 546, A71
 Fabrycky, D. C., Lissauer, J. J., Ragozzine, D., et al. 2014, *ApJ*, 790, 146
 Fang, J. & Margot, J.-L. 2012, *ApJ*, 761, 92
 Fendyke, S. M. & Nelson, R. P. 2014, *MNRAS*, 437, 96
 Frank, J., King, A., & Raine, D. 1992, *Accretion power in astrophysics*.
 Fressin, F., Torres, G., Charbonneau, D., et al. 2013, *ApJ*, 766, 81
 Ghosh, P. & Lamb, F. K. 1979, *ApJ*, 232, 259
 Gladman, B. 1993, *Icarus*, 106, 247
 Goldreich, P. & Schlichting, H. E. 2014, *AJ*, 147, 32
 Goldreich, P. & Tremaine, S. 1979, *ApJ*, 233, 857
 Goldreich, P. & Tremaine, S. 1980, *ApJ*, 241, 425
 Hansen, B. M. S. & Murray, N. 2012, *ApJ*, 751, 158
 Hartmann, L., Calvet, N., Gullbring, E., & D'Alessio, P. 1998, *ApJ*, 495, 385
 Henrard, J. & Lemaître, A. 1983, *Icarus*, 55, 482
 Howard, A. W., Marcy, G. W., Bryson, S. T., et al. 2012, *ApJS*, 201, 15
 Johansen, A., Davies, M. B., Church, R. P., & Holmelin, V. 2012, *ApJ*, 758, 39
 Johns-Krull, C. M. 2007, *ApJ*, 664, 975
 Johns-Krull, C. M., Chen, W., Valenti, J. A., et al. 2013, *ApJ*, 765, 11
 Kley, W. & Nelson, R. P. 2012, *ARA&A*, 50, 211
 Koenigl, A. 1991, *ApJ*, 370, L39
 Lai, D., Foucart, F., & Lin, D. N. C. 2011, *MNRAS*, 412, 2790
 Lee, M. H., Fabrycky, D., & Lin, D. N. C. 2013, *ApJ*, 774, 52
 Lee, M. H. & Peale, S. J. 2002, *ApJ*, 567, 596
 Lin, D. N. C. & Papaloizou, J. 1979, *MNRAS*, 186, 799
 Lin, D. N. C. & Papaloizou, J. C. B. 1993, in *Protostars and Planets III*, ed. E. H. Levy & J. I. Lunine, 749–835
 Lipunov, V. M. & Shakura, N. I. 1980, *Soviet Astronomy Letters*, 6, 28
 Lithwick, Y. & Wu, Y. 2012, *ApJ*, 756, L11
 Lithwick, Y., Xie, J., & Wu, Y. 2012, *ApJ*, 761, 122
 Liu, B., Zhang, X., & Lin, D. N. C. 2016, *ApJ*, 823, 162
 Liu, B., Zhang, X., Lin, D. N. C., & Aarseth, S. J. 2015, *ApJ*, 798, 62
 Lopez, E. D. & Fortney, J. J. 2014, *ApJ*, 792, 1
 Mamajek, E. E. 2009, in *American Institute of Physics Conference Series*, Vol. 1158, *American Institute of Physics Conference Series*, ed. T. Usuda, M. Tamura, & M. Ishii, 3–10
 Marcy, G. W., Isaacson, H., Howard, A. W., et al. 2014, *ApJS*, 210, 20
 Mayor, M., Marmier, M., Lovis, C., et al. 2011, *ArXiv e-prints*: 1109.2497
 McNeil, D. S. & Nelson, R. P. 2010, *MNRAS*, 401, 1691
 McQuillan, A., Mazeh, T., & Aigrain, S. 2014, *ApJS*, 211, 24
 Mills, S. M., Fabrycky, D. C., Migaszewski, C., et al. 2016, *Nature*, 533, 509
 Morbidelli, A. & Raymond, S. N. 2016, *ArXiv e-prints*: 1610.07202
 Mulders, G. D., Pascucci, I., & Apai, D. 2015, *ApJ*, 798, 112
 Murray, C. D. & Dermott, S. F. 1999, *Solar system dynamics*
 Ogihara, M., Duncan, M. J., & Ida, S. 2010, *ApJ*, 721, 1184
 Ogihara, M. & Ida, S. 2009, *ApJ*, 699, 824
 Ogihara, M. & Kobayashi, H. 2013, *ApJ*, 775, 34
 Ogihara, M., Morbidelli, A., & Guillot, T. 2015, *A&A*, 578, A36
 Ormel, C. W. 2013, *MNRAS*, 428, 3526
 Paardekooper, S.-J., Baruteau, C., Crida, A., & Kley, W. 2010, *MNRAS*, 401, 1950
 Paardekooper, S.-J., Baruteau, C., & Kley, W. 2011, *MNRAS*, 410, 293
 Paardekooper, S.-J. & Papaloizou, J. C. B. 2009a, *MNRAS*, 394, 2297
 Paardekooper, S.-J. & Papaloizou, J. C. B. 2009b, *MNRAS*, 394, 2297
 Papaloizou, J. C. B. & Szuszkiewicz, E. 2005, *MNRAS*, 363, 153
 Petigura, E. A., Howard, A. W., & Marcy, G. W. 2013, *Proceedings of the National Academy of Science*, 110, 19273
 Petrovich, C., Malhotra, R., & Tremaine, S. 2013, *ApJ*, 770, 24
 Pierens, A. & Nelson, R. P. 2008, *A&A*, 482, 333
 Rein, H. 2012, *MNRAS*, 427, L21
 Rogers, L. A. 2015, *ApJ*, 801, 41
 Romanova, M. M., Ustyugova, G. V., Koldoba, A. V., & Lovelace, R. V. E. 2002, *ApJ*, 578, 420
 Romanova, M. M., Ustyugova, G. V., Koldoba, A. V., & Lovelace, R. V. E. 2004, *ApJ*, 610, 920
 Romanova, M. M., Ustyugova, G. V., Koldoba, A. V., Wick, J. V., & Lovelace, R. V. E. 2003, *ApJ*, 595, 1009
 Shabram, M., Demory, B.-O., Cisewski, J., Ford, E. B., & Rogers, L. 2016, *ApJ*, 820, 93
 Shakura, N. I. & Sunyaev, R. A. 1973, *A&A*, 24, 337
 Steffen, J. H. & Hwang, J. A. 2015, *MNRAS*, 448, 1956
 Suzuki, T. K., Muto, T., & Inutsuka, S.-i. 2010, *ApJ*, 718, 1289
 Tanaka, H., Takeuchi, T., & Ward, W. R. 2002, *ApJ*, 565, 1257
 Terquem, C. & Papaloizou, J. C. B. 2007, *ApJ*, 654, 1110
 Ward, W. R. 1997, *Icarus*, 126, 261

- Wardle, M. 2007, *Ap&SS*, 311, 35
Williams, J. P. & Cieza, L. A. 2011, *ARA&A*, 49, 67
Winn, J. N. & Fabrycky, D. C. 2015, *ARA&A*, 53, 409
Wolfgang, A., Rogers, L. A., & Ford, E. B. 2016, *ApJ*, 825, 19
Xie, J.-W. 2014, *ApJ*, 786, 153
Xie, J.-W., Dong, S., Zhu, Z., et al. 2016, *Proceedings of the National Academy of Science*, 113, 41
Yang, H. & Johns-Krull, C. M. 2011, *ApJ*, 729, 83